ChemComm

COMMUNICATION

View Article Online
View Journal | View Issue

Cite this: *Chem. Commun.*, 2025, **61**, 3163

Received 1st December 2024,
Accepted 20th January 2025

DOI: 10.1039/d4cc06356b

rsc.li/chemcomm

Construction of a laccase/CeO_2/attapulgite nanocomposite for photoenzymatic catalytic CO_2 reduction coupled with biomass oxidation†

Huaimin Tian, Yao Xiao, Chao Yao, Taoli Huhe* and Xiazhang Li *

Herein, a photoenzymatic synergistic catalytic material, *i.e.* laccase/CeO_2/attapulgite, was prepared for simultaneous CO_2 conversion and biomass conversion. Based on the synergistic effect of the photoenzyme in the prepared composites, a remarkable CO (27.15 μmol g_{cat}^{-1} h^{-1}) and CH_4 (64.88 μmol g_{cat}^{-1} h^{-1}) production rate and a benzaldehyde yield of 84.1% were gained.

With the tremendous use of fossil fuels such as oil and natural gas, the rapid growth of CO_2 emissions has directly led to global warming and increased the possibility of extreme weather events.[1–3] In order to cope with these environmental challenges, many strategies have been proposed and implemented, including pyrolysis, electrochemical conversion[4] and photochemical processes.[5–7] At the same time, in order to meet the goal of carbon neutrality, reducing the concentration of CO_2 in the atmosphere or converting it into renewable energy is promising.[8,9] Solar-driven chemical conversion has created an indispensable low-carbon manufacturing system that uses abundant solar energy to provide power for the breaking and rearrangement of chemical bonds at ambient temperature and pressure.[10,11]

However, in the conventional photocatalytic CO_2 reduction system, the oxidation half-reaction is usually the oxygen evolution reaction (OER), in which oxygen is generated as the main product and it suffers from sluggish kinetics.[12,13] Therefore, only the reduction half-reaction has economic value, which indicates that only the photoexcited electrons (e^-) rather than all electron–hole pairs are effectively utilized.[14,15] In particular, the selective photocatalytic oxidation of benzyl alcohol (BA) to benzaldehyde (BAD), emerges as a promising process that garners increasing attention.[16–18] Compared to traditional industrial methods, this process benefits from clean and mild operating conditions.[19–21] Furthermore, BAD serves as a valuable precursor for the preparation of various basic drugs, vitamins, cosmetics, and fragrances.[22,23] In this regard, designing an efficient bifunctional photocatalyst capable of driving both CO_2 reduction and the oxidation of BA to BAD in an environmentally friendly aqueous solution is not only practically necessary, but also aligns with economic and ecological considerations.

As a natural clay mineral, attapulgite is characterized by its high content of hydrous magnesium aluminum silicate. It has a unique rod-like structure and large specific surface area, which can provide sufficient loading sites for metal oxides or metals.[24,25] CeO_2 is an excellent semiconductor photocatalyst with good stability and catalytic performance. It has been used as an active component in the field of industrial catalysis.[26,27] When CeO_2 was loaded on attapulgite, on the one hand, it greatly enhances the stability and photocatalytic activity of the semiconductor; on the other hand, it also reduces the agglomeration of the catalyst and improves the contact area between the active site (Ce^{3+}/Ce^{4+}) and the reactant, which is conducive to the photocatalytic reduction reaction.[28–30] Laccase, as a member of the oxidoreductase family, possesses an active site with four copper ions, three of which are Cu(II), capable of catalyzing the oxidation of phenolic and certain non-phenolic compounds by accepting electrons and transferring them to oxygen, resulting in the formation of water or other oxidation products.[31] It exhibits a high redox potential, enabling it to undergo reduction reactions with substrates upon electron acquisition.[32–34] Photoenzyme synergistic catalysis emerges as an innovative catalytic strategy that combines the advantages of photocatalysis and bioenzyme catalysis to achieve efficient conversion of specific substrates under mild conditions.[35] In this process, photosensitizers absorb light energy to excite electrons to high energy states, which are then transferred to the active center of the enzyme to activate the enzyme and promote the redox reaction of the substrate.[36] Recently, Reisner *et al.* have pioneered the combination of TiO_2 and formate dehydrogenase (FDH) to synergistically catalyze the degradation of cellulose and the reduction of CO_2.[37] To the best of our knowledge, there has been no report on mineral-based

National-Local Joint Engineering Research Center of Biomass Refining and High-quality Utilization, Changzhou Key Laboratory of Biomass Green, Safe & High Value Utilization, Changzhou University, Changzhou 213164, P. R. China.
E-mail: xiazhang@cczu.edu.cn, hhtaoli@cczu.edu.cn

† Electronic supplementary information (ESI) available. See DOI: https://doi.org/10.1039/d4cc06356b

photoenzyme synergistic catalysis, which combines the advantage of mineral and enzyme characteristics.

In this work, as shown in Fig. S1 (ESI†), we prepared various photoenzyme composites with different laccase loadings for both CO_2 reduction and biomass valorisation. In this photoenzymatic catalytic system, CO_2 reduction produces important syngas components such as CO and CH_4, and the selected biomass substrate benzyl alcohol was selectively oxidized to benzaldehyde. The addition of laccase led to the enhancement in photoelectrochemical properties and photocatalytic properties of the composites. Compared with CeO_2/ATP, the participation of biological enzymes significantly increased the yield of reduction products. This new type of photoenzyme catalytic system can effectively utilize photogenerated holes (h^+) and electrons (e^-), and improve the utilization efficiency of photogenerated carriers. This study has important implications for the design of photoenzyme synergistic catalysts.

Fig. 1a shows the X-ray diffraction (XRD) crystal structure of the samples. For pure ATP, the characteristic diffraction peaks appear at 8.1° in line with the corresponding (110) plane.[38] After acid treatment, the basic silicon-oxygen tetrahedral chain layered structure of ATP is still preserved, but the main characteristic peak is significantly weakened and moves to a higher angle.[39] After loading CeO_2, the cubic phase appears, showing the characteristic peaks of CeO_2, indicating that CeO_2 has been successfully loaded onto the surface of ATP.[40] However, in the subsequent melamine (MEL) modification, due to the overlapping of the characteristic peaks of CeO_2 and some characteristic peaks of MEL, the peak of CeO_2 in the subsequent samples is not obvious, and the intensity of the characteristic peaks of ATP and CeO_2 decreases. This can be due to the fact CeO_2/p-ATP and MEL form an intimate composite.[40] The characteristic crystal plane of melamine appears in the sample (MEL)/CeO_2/p-ATP, indicating the successful loading of MEL.[41] After enzyme immobilization, no obvious peak shape change is observed, suggesting that the immobilization of the enzyme does not cause further changes in the crystallinity of the nanocomposites.[34] However, as the amount of immobilized enzyme increases, other characteristic peaks are gradually covered up, which cannot be clearly identified.[42]

In order to analyze the functional groups and bonding states of the composites, FT-IR spectroscopy analysis is performed, as shown in Fig. 1b. In the FT-IR spectrum of pure ATP, the peaks at 3620 cm^{-1} and 3570 cm^{-1} are attributed to the stretching vibration of Al–OH–Si, and the peaks at 1031 cm^{-1} and 983 cm^{-1} correspond to Si–O–Si asymmetric stretching and Si–O stretching vibration, respectively.[43] After acidification of ATP, the Al–OH–Si stretching vibration peak is weakened, which may be caused by the exchange of aluminum atoms with H^+, and the Si–O–Si peak at 1031 cm^{-1} is shifted, indicating that acidification changes the ATP structure.[44] After MEL modification, the peaks at 3570 cm^{-1} and 1653 cm^{-1} are weakened, indicating that some functional groups of MEL are combined with ATP through hydrogen bonds, and the π-electron of MEL may promote the bonding with ATP. The peaks at 3469 cm^{-1} and 3419 cm^{-1} correspond to the asymmetric stretching vibration of NH_2, indicating that MEL is successfully loaded. The peaks at 1650 cm^{-1}, 1550 cm^{-1} and 1435 cm^{-1} correspond to the triazine ring vibration.[40] The stretching vibrations of –OH and –NH_2 have overlap at 3200–3600 cm^{-1}, and the peak width is affected by hydrogen bonds.[41] The peak at 2930 cm^{-1} is attributed to the aliphatic C–H stretching vibration, suggesting that Lac has been successfully loaded.

The morphology and microstructure of the prepared composites are characterized by TEM, as shown in Fig. 2 The original ATP exhibits a uniform one-dimensional rod-like structure (Fig. 2a). After acidification, ATP still maintains a rod-like structure with a diameter of about 30–40 nm (Fig. 2b), and the structure becomes well-dispersed, which is due to the replacement of some cations between the layers by H^+. After loading CeO_2, the surface of ATP is uniformly covered with 3–8 nm CeO_2 nanoparticles without agglomeration (Fig. 2c), as evidenced by the HRTEM in Fig. S2 (ESI†) and the morphology of ATP has no obvious change. After MEL modification, the diameter of the composite material increases to 20–50 nm (Fig. 2d–f), indicating that MEL is successfully deposited on ATP and grows along the surface of ATP without a dense accumulation layer, confirming that MEL is uniformly fixed on the surface of ATP. SEM further analyzes the loading of Lac on p-ATP (Fig. 2g). SEM-EDS element mapping (Fig. 2h–i) shows that carbon and copper elements are evenly distributed, confirming the successful loading of Lac.

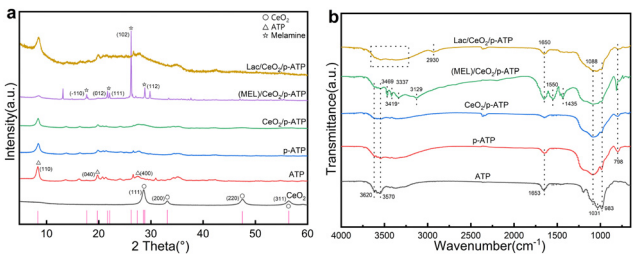

Fig. 1 (a) The XRD patterns and (b) FT-IR spectra of various photocatalysts.

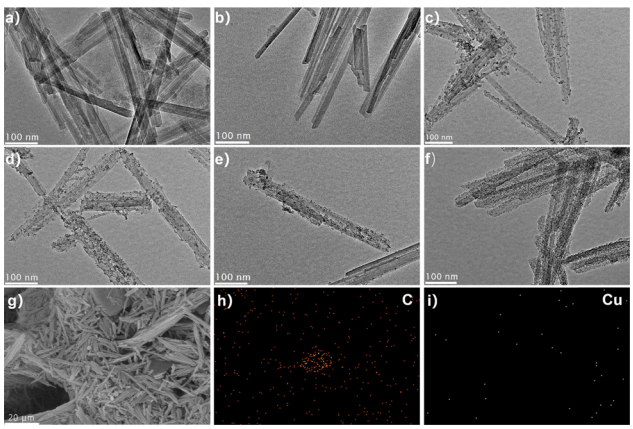

Fig. 2 TEM images of (a) ATP, (b) p-ATP, (c) CeO_2/p-ATP, (d) 0.5-Lac/CeO_2/p-ATP, (e) 1.0-Lac/CeO_2/p-ATP and (f) 2.0-Lac/CeO_2/p-ATP. (g) SEM image, (h) and (i) EDX elemental mapping of 1.0-Lac/CeO_2/p-ATP.

The UV-Vis spectra of the samples are shown in Fig. 3a. The absorption peaks of ATP and p-ATP appear at about 255 nm, which may be related to the chemical bonds between the oxygen atoms and metal atoms, indicating that ATP has a certain UV absorption capacity. In the rest of the samples loaded with CeO_2, the absorption peak appears at about 330 nm, which can be attributed to the charge transfer between O 2p and Ce 4f states in O^{2-} and Ce^{4+} and the charge transfer between 4f1 and 5d1 states in Ce^{3+}, resulting in the UV absorption of the cerium oxide.[45]

The photogenerated electron–hole separation efficiency of the Lac/CeO_2/ATP composites with different loadings is studied by electrochemical characterization. Fig. 3b shows that compared with p-ATP and CeO_2/p-ATP, the composites with Lac loading show stronger photocurrent response, indicating that the enzyme loading enhances the photogenerated carrier separation efficiency of CeO_2/p-ATP. However, when the enzyme loading exceeds the optimal value, the photocurrent intensity decreases, which may be due to the fact that excessive enzyme loading has agglomeration affecting light absorption. The EIS impedance analysis of Fig. 3c shows that the impedance of p-ATP is the largest, while the impedance of the enzyme-loaded composites is small, and the impedance is the lowest at the optimal loading of 1.0-Lac/CeO_2/p-ATP, which confirms that the addition of enzyme increases the carrier mobility. When the loading amount is larger than 1.0, the photocurrent response is weakened and the electrochemical impedance is increased, which is attributed to the fact that the excessive enzyme loading affects the light absorption of CeO_2. Photoluminescence (PL) spectroscopy is employed to reveal the charge recombination of the photocatalysts (Fig. 3d). It can be clearly observed that the PL intensity of the Lac-loaded sample is much lower than that of other samples, indicating that the charge recombination in the composite is suppressed.

Fig. 4a reveals the effect of different Lac loadings on the CO and CH_4 production. In the CeO_2/p-ATP composite, the yields of CO and CH_4 are 14.28 μmol g_{cat}^{-1} h^{-1} and 52.42 μmol g_{cat}^{-1} h^{-1}, respectively, which are attributed to the catalytic activity of CeO_2

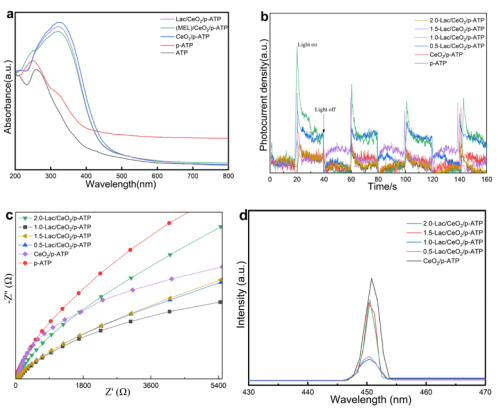

Fig. 3 Optical and photoelectrochemical properties of various photocatalysts: (a) UV-vis patterns, (b) EIS, (c) transient photocurrent responses and (d) PL spectra.

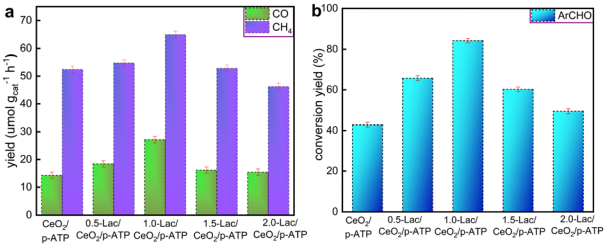

Fig. 4 Photocatalytic properties of various photocatalysts: (a) production yield of CO and CH_4, and (b) conversion yield of ArCHO.

and its loading on p-ATP enhances the contact between active sites and substrates. As for 0.5-Lac/CeO_2/p-ATP, the yield increase is not significant, which may be due to the insufficient amount of enzyme and the three-dimensional structure limiting the exchange of the substrate and product. When it comes to 1.0-Lac/CeO_2/p-ATP, the yields of CO and CH_4 are significantly increased to 27.15 μmol g_{cat}^{-1} h^{-1} and 64.88 μmol g_{cat}^{-1} h^{-1}, respectively. Meanwhile, the conversion yield of benzyl alcohol also reaches the maximum of 84.1% (Fig. 4b). However, for the composite 1.5-Lac/CeO_2/p-ATP, the yield decreases, which may be due to the inhibition of light absorption and carrier generation by excessive enzyme loading; in addition, the unfixed enzyme may have a negative effect on light absorption. In addition, as shown in Fig. S5 (ESI†), the 1.0-Lac/CeO_2/p-ATP composite still maintains good catalytic activity after five cycles of testing. Meanwhile, the tracking experiment of the 1.0-Lac/CeO_2/p-ATP composite was also carried out in a CO_2 atmosphere and N_2 atmosphere, respectively, and the reduction products of the comparative experiments were detected by gas chromatography, as shown in Fig. S6 (ESI†). Notably, the target gaseous product is not detected in the N_2 atmosphere, suggesting that CO and CH_4 are evidently derived from CO_2.

Based on the above analysis, the possible mechanism of CO_2 reduction by Lac/CeO_2/ATP is proposed, as shown in Fig. S3 (ESI†). Meanwhile, in order to explore the adsorption and conversion process of the reaction intermediates in the photocatalytic process, the *in situ* DRIFTS characterization of the photocatalytic CO_2 coupling with benzyl alcohol reaction was carried out using the sample 1.0-Lac/CeO_2/ATP, as shown in Fig. S4 (ESI†). Under the excitation of light, CeO_2 absorbed photons to produce photocarriers, and then photoelectrons are quickly transferred to the surface of the catalyst. After electron transfer, the active center Cu(II) of Lac undergoes a reduction reaction to form Cu(III), and all four active sites of Lac are converted to Cu(III) in the subsequent reaction.[31] In the dark reaction, CO_2 is adsorbed on the surface of the composite, which improves the contact efficiency of Lac and CO_2. CO_2 readily accesses its active site *via* the channel structure of Lac, facilitating the formation of an enzyme–CO_2 complex, which reduces CO_2 to CO. However, the produced CO is not promptly released into the external environment through the porous structure of Lac, leading to a recombination of some generated CO with the active site of Lac to re-form the enzyme–CO complex. Subsequently, this complex is further reduced to CH_4 under proton influence.

In summary, a series of ternary Lac/CeO_2/ATP composites were prepared by homogeneous precipitation and covalent cross-linking. Self-immobilization of Lac onto CeO_2/ATP formed a photo-enzyme system, leading to fast charge separation and migration, synergistically boosted CO_2 reduction and biomass-derived benzyl alcohol conversion. Moreover, this novel photo-enzyme realized the integrated utilization of the photo-generated charges as well as the redox reaction, enabling the simultaneous production of CO/CH_4 gas and benzaldehyde.

Huaimin Tian: writing – original draft; investigation, Yao Xiao: data curation, Chao Yao: formal analysis, TaoLi Huhe: validation; resources, Xiazhang Li: writing – review & editing; Conceptualization; project administration.

This work was supported by the National Natural Science Foundation of China (51674043). We thank the Analysis and Testing Center of Changzhou University for the characterization.

Data availability

The data supporting this article have been included as part of the ESI.†

Conflicts of interest

There are no conflicts to declare.

Notes and references

1 T. Y. Li, P. Wang, M. He, T. B. Zhang, C. Yang and Z. X. Li, *Coord. Chem. Rev.*, 2024, **521**, 216179.
2 J. Ran, M. Jaroniec and S. Z. Qiao, *Adv. Mater.*, 2018, **30**, 1704649.
3 Y. Chen, D. Wang, X. Deng and Z. Li, *Catal. Sci. Technol.*, 2017, **7**, 4893–4904.
4 R. Yanagi, T. Zhao, M. Cheng, B. Liu, H. Su, C. He, J. Heinlein, S. Mukhopadhyay, H. Tan, D. Solanki and S. Hu, *J. Am. Chem. Soc.*, 2023, **145**, 15381–15392.
5 Y. Zhang and H. Liang, *Adv. Compos. Hybrid Mater.*, 2024, **7**, 21.
6 X. Li, J. Yu, M. Jaroniec and X. Chen, *Chem. Rev.*, 2019, **119**, 3962–4179.
7 D. D. Li, M. Kassymova, X. C. Cai, S. Q. Zang and H. L. Jiang, *Coord. Chem. Rev.*, 2020, **412**, 213262.
8 D. Zhang, Y. Li, Y. Li and S. Zhan, *SmartMat*, 2022, **3**, 417–446.
9 L. Liu, Z. Wang, J. Zhang, O. Ruzimuradov, K. Dai and J. Low, *Adv. Mater.*, 2023, **35**, e2300643.
10 A. V. Puga, *Coord. Chem. Rev.*, 2016, **315**, 1–66.
11 M. Tudor, R. Borlan, D. Maniu, S. Astilean, M. L. de la Chapelle and M. Focsan, *Sci. Total Environ.*, 2024, **932**, 172792.
12 G. Liu, Y. Xu, T. Yang and L. Jiang, *Nano Mater. Sci.*, 2023, **5**, 101–116.
13 W. M. Tong, M. Förster, F. Dionigi, S. Dresp, R. S. Erami, P. Strasser, A. J. Cowan and P. Farràs, *Nat. Energy*, 2020, **5**, 367–377.
14 Z. Chen, Q. C. Li, H. M. Xiang, Y. Wang, P. F. Yang, C. L. Dai, H. D. Zhang, W. P. Xiao, Z. X. Wu and L. Wang, *Inorg. Chem. Front.*, 2023, **10**, 1493–1500.
15 Q. Li, X. Luan, Z. Xiao, W. Xiao, G. Xu, Z. Li, Z. Wu and L. Wang, *Inorg. Chem.*, 2023, **62**, 9687–9694.
16 T. Zhu, X. Ye, Q. Zhang, Z. Hui, X. Wang and S. Chen, *J. Hazard. Mater.*, 2018, **367**, 277–285.
17 L.-M. Zhao, Q.-Y. Meng, X.-B. Fan, C. Ye, X.-B. Li, B. Chen, V. Ramamurthy, C.-H. Tung and L.-Z. Wu, *Angew. Chem., Int. Ed.*, 2017, **56**, 3020–3024.
18 Q. Yang, T. Wang, Z. Zheng, B. Xing, C. Li and B. Li, *Appl. Catal., B*, 2022, **315**, 121575.
19 X. Lang, J. Zhao and X. Chen, *Chem. Soc. Rev.*, 2016, **45**, 3026–3038.
20 Z. Bao, L. Jun, G. Yuying, C. Ruifeng, W. Zhiliang, G. Lin, Z. Xianwen and L. Can, *J. Catal.*, 2016, **345**, 96–103.
21 J. Zhang, S. Meng, X. Ye, C. Ling, S. Zhang, X. Fu and S. Chen, *Appl. Catal., B*, 2017, **218**, 420–429.
22 Y. Liu, P. Zhang, B. Tian and J. Zhang, *ACS Appl. Mater. Interfaces*, 2015, **5**, 3760–3766.
23 P. Li, H. Zhao, X. Yan, X. Yang, J. Li, S. Gao and R. Cao, *Sci. China Mater.*, 2020, **242**, 302–311.
24 W. Shenjin, L. Xiaoxi, Z. Chenyang, H. Wenjihao, L. Yaochi, F. Xinzhuang, Y. Jun and S. Wei, *Sep. Purif. Technol.*, 2025, **353**, 128377.
25 Y. Tian, S. Li and G. Zhang, *J. Environ. Chem. Eng.*, 2024, **12**, 113641.
26 A. E. Herzog, T. J. Michael, A. D. Dunkelberger, M. D. Johannes, D. R. Rolison, P. A. DeSario and T. G. Novak, *Nanoscale*, 2024, **16**, 9659–9679.
27 S. H. Cao, J. R. Qu, Y. Q. Zhao, Y. T. Sun, W. T. Gao, B. Han and Y. Lu, *Rare Met.*, 2024, **43**, 3134–3145.
28 J. You, F. Chen, X. B. Zhao and Z. G. Chen, *J. Rare Earths*, 2010, **28**, 347–352.
29 J. Huang, X. H. Ye, W. J. Li, A. Q. Shi, X. N. Chu, Z. W. Cao, C. Yao and X. Z. Li, *J. Ind. Eng. Chem.*, 2022, **116**, 504–514.
30 Z. Ma, Y. Li, Z. Li, Z. Liu, X. Wang, Y. Tan, X. Chen, W. Lu and Y. Ding, *Chem. Eng. J.*, 2024, **497**, 154592.
31 V. Madhavia and S. S. Lele, *BioResources*, 2009, **4**, 1694–1717.
32 S. Zhang, Z. Dong, J. Shi, C. Yang, Y. Fang, G. Chen, H. Chen and C. Tian, *Bioresour. Technol.*, 2022, **361**, 127699.
33 Z. Li, Z. Chen, Q. Zhu, J. Song, S. Li and X. Liu, *J. Hazard. Mater.*, 2020, **399**, 123088.
34 M. Tharmavaram, G. Pandey, P. Bhatt, P. Prajapati, D. Rawtani, K. P. Sooraj and M. Ranjan, *Int. J. Biol. Macromol.*, 2021, **191**, 1046–1055.
35 S. H. Li, J. F. Shi, S. S. Liu, W. P. Li, Y. Chen, H. T. Shan, Y. Q. Cheng, H. Wu and Z. Y. Jiang, *Chin. J. Catal.*, 2023, **44**, 96–110.
36 R. Jiang, G. Luo, G. Chen, Y. Lin, L. Tong, A. Huang, Y. Zheng, Y. Shen, S. Huang and G. Ouyang, *Sci. Adv.*, 2024, **10**, eadp1796.
37 E. Lam, M. Miller, S. Linley, R. R. Manuel, I. A. C. Pereira and E. Reisner, *Angew. Chem., Int. Ed.*, 2023, 62, e202215894.
38 S. Y. Xue, B. F. Li, P. Mu and J. Li, *Prog. Org. Coat.*, 2022, **170**, 106966.
39 T. X. Wu, X. Tang, Y. Lin, Y. R. Wang, S. J. Ma, Y. Xue, H. Q. Ren and K. Xu, *Chem. Eng. J.*, 2024, **486**, 150079.
40 J. Peng, H. Sun, J. Wang, F. Qiu, P. Zhang, W. Ning, D. Zhang, W. Li, C. Wei and S. Miao, *ACS Appl. Mater. Interfaces*, 2021, **13**, 10933–10941.
41 P. Negro, F. Cesano, A. Damin, R. Brescia and D. Scarano, *J. Alloys Compd.*, 2024, **1002**, 175053.
42 H. Zhao, F. X. Qiu, J. Yan, J. Wang, X. Li and D. Y. Yang, *Appl. Clay Sci.*, 2016, **121**, 137–145.
43 H. C. Yang, Z. N. Cai, H. T. Liu, Z. Cao, Y. P. Xia, W. Z. Ma, F. H. Gong, G. L. Tao and C. L. Liu, *Mater. Chem. Phys.*, 2020, **241**, 122334.
44 X. Li, H. Zhang, H. Lu, S. Zuo, Y. Zhang and C. Yao, *Environ. Sci. Pollut. Res.*, 2019, **26**, 12842–12850.
45 K. Hamidian, M. R. Saberian, A. Miri, F. Sharifi and M. Sarani, *Ceram. Int.*, 2021, **47**, 13895–13902.

